Research Article
Vol. 14, No. 7 / 1 Jul 2023 / *Biomedical Optics Express* 3775
Biomedical Optics EXPRESS

Fractal-based aberration-corrected full-field OCT

YUE ZHU,[1,*] YUAN ZHOU,[2] AND ZHENYAN GUO[1]

[1] *Department of Optical Engineering, Nanjing University of Science and Technology, 200 Xiao Ling Wei, Nanjing, 210094, China*
[2] *Department of Vascular Surgery, Sir Run Run Shaw Hospital, Zhejiang University School of Medicine, Hangzhou, Zhejiang 310020, China*
https://milkshakism.cloud/lab/
[*] *zhuyue@njust.edu.cn*

Abstract: The Kolmogorov turbulence model has been validated as a quantitative 3D light scattering model of the inhomogeneous refraction index of biological tissue using full-field OCT (FF-OCT). A fractal-based computational compensation approach was proposed for correcting of depth-resolved aberrations with volumetric FF-OCT. First, the power-spectral density spectrum of the index inhomogeneities was measured by radial Fourier transformation of volumetric data. The spectrum's shape indicates the spatial correlation function and can be quantified as the fractal dimension of tissue. The defocusing correction matrix was built by applying fractal-based analysis as an image quality metric. For comparison, tissue-induced in-depth aberration models were built by phase compensation. After digital aberration correction of FF-OCT images, it enables extracting the temporal contrast indicating the sample dynamics in onion in mitosis and *ex vivo* mouse heart during delayed neuronal death. The proposed fractal-based contrast augmented images show subcellular resolution recording of dynamic scatters of the growing-up onion cell wall and some micro activities. In addition, low-frequency chamber and high-frequency cardiac muscle fibers from *ex vivo* mouse heart tissue. Therefore, the depth-resolved changes in fractal parameters may be regarded as a quantitative indicator of defocus aberration compensation. Also the enhanced temporal contrast in FF-OCT has the potential to be a label-free, non-invasive, and three-dimensional imaging tool to investigate sub-cellular activities in metabolism studies.

© 2023 Optica Publishing Group under the terms of the Optica Open Access Publishing Agreement

1. Introduction

Full-field optical coherence tomography (FF-OCT) has shown its high-resolution capability of generating sub-cellular resolution *en face* tomographic images of *in vitro* or *in vivo* tissues, making it possible to quantitative morphological difference between benign and cancerous tumor lesions. Recently, many research groups have tried to model the imaging properties, a correctly quantitative parameter from *en face* images and explore the possible applications in disease diagnosis by parallelized detection of depth information [1–3]. In addition, laterally paralleled Fourier-domain OCT (FD-OCT) techniques have also shown remarkable volumetric imaging capabilities during a single sweep, and it has been going beyond those of scanning FD-OCT systems, namely full-field swept-source optical coherence tomography [4–7].

The quantitative modeling of the imaging signal of pathological and healthy areas is necessary to improve the specificity of diagnosis with tomographic *en face* images obtained with FF-OCT. Several models have been proposed to understand the imaging properties of FF-OCT by either angular spectrum concept or Fourier transform-based coherence consideration [8–12]. All the models mentioned above have a limitation in that, in their analysis, the sample was assumed to be a plane-reflective surface or a layered sample. Recently, Gao considered the effects of both temporal and spatial coherence on resolution in FF-OCT and also modeled interference signal with three-dimensional sample structures and its quantitative fractal properties [13]. This model

#485090
Journal © 2023
https://doi.org/10.1364/BOE.485090
Received 9 Jan 2023; revised 15 Jun 2023; accepted 15 Jun 2023; published 27 Jun 2023

is based on the hypothesis that tissue can be regarded as a random scattering medium with the structure of the refractive-index inhomogeneities [14,15]. It was also proposed to use fractal dimension as a quantitative measure for distinguishing the different tissue types in FF-OCT images.

Although fractal parameters can be used to identify the subtle variations in tissue and organ at the early stage of the diseases, one open issue in FF-OCT is the defocus effect. When a light beam is focused on a deeper region within a tissue, the refraction of light at the tissue surface causes the actual focus of the objective lenses to shift deeper (forward) into the sample with respect to the nominal focus, whereas the coherence plane moves backward. In addition to the displacement of the focus, other aberrations also influence characteristics of the light distribution in the focus region and blur image contrast in FF-OCT.

The depth-resolved wavefront aberration correction was first proposed in Fourier-domain OCT. Yasuno et al. demonstrated defocus correction for depth of field extension in OCT that applies numerical phase correction, which relies on Fresnel wave propagation and knowledge of system geometry [16]. G.Hüttmann et al. present a unified dispersion/aberration correction which is based on a polynomial parameterization of the phase error and an optimization of the image quality using Shannon's entropy [17,18]. The theoretical model paves the way towards computational aberration correction for high-resolution and deep imaging of biological tissues in FF-OCT [1]. First, Gao et al. present the contrast reduction mechanism and interpretation in FF-OCT images [19]. Then, A. Dubois proposed the mechanism compensation for the defocus effect due to the mismatch of focal and coherence plane by extending reference arm [20,21]. Recently, Victor et al. reported on a theoretical model for image formation in FF-OCT [22]. Several works have tried digital depth-resolved aberration correction methods for FF-OCT. Labiau et al. tried parallel detection with the help of FF-OCT, this problem can be avoided, and phase stability can be maintained across the lateral plane. Numerical defocus correction in FF-OCT has been implemented based on wave propagation and modeling of system geometry [23]. Min et al. proposed a numerical correction method to rejuvenate the degraded OCT images. The method uses the phase-shifting digital holographic technique based on the Fresnel-Kirchhoff diffraction theory, which numerically relocates the defocused sample at the virtual focal plane. Ideally, a fully focused OCT image can be constructed regardless of the degree of optical distortion along the depth of the sample [24]. Marie et al. demonstrated that the frequency content of FF-OCT image spectra in signal-to-noise ratio and the cutoff frequency is degraded by aberrations but remains much higher than in conventional incoherent images [25]. The digital depth-resolved aberration correction methods were also present in high-speed Fourier-domain FF-OCT. Kumar et al. employed a 4-f telecentric imaging system to detect and correct wavefront aberration in the pupil plane by sub-aperture correlation as a post-processing technique for full-field swept-source OCT [26,27]. Boppart et al. modeled the process of aberration correction as a filtering operation on the aberrant image using a phase filter in the Fourier domain and obtains truly coherent three-dimensional tomograms of the living human retina with high image quality [28]. Maciej et al. modulated the signal after coherent averaging, and it preserves lateral phase stability. This enables computational phase correction to compensate for geometrical aberrations [29].

Nevertheless, the layered structure model is the most used in the mentioned depth-resolved aberration correction methods, which cause the changes in scattering light only between layers [30,31]. It is evident that the layered structure model is not appropriate for describing the imaging performance of FF-OCT because it has micron- or submicron-resolution in three-dimensions. In addition, OCT measures the local microstructural inhomogeneity and anisotropy when considering a 3D light scattering model that has been demonstrated theoretically and experimentally by Pan et al. [32]. Therefore, a 3D inhomogeneity and anisotropy light scattering model in depth-resolved aberration correction for FF-OCT is necessary.

Second, the mentioned aberration compensation methods cannot compensate for the high-order aberration that interacts with defocus. This is because the PSF (Point spread function) of scanning OCT is an inverse Fourier transform of autocorrelation of illumination pupil function and collection pupil function. The phase error of OCT signal in the spatial frequency domain due to aberrations is not the same as the single-pass wavefront error. Only in the case of full-field or line-field illumination and collection system, the illumination mode along the imaging direction (perpendicular to scanning direction in the case of LF-OCT) is a single plane wave [33]. Hence, the entrance pupil functions no longer depend on the focus point. Therefore, an invariant and quantitative image quality metric can correct not only single but also high-order aberrations in the case of full-field illumination. Moreover, Shannon's entropy was employed as an image quality metric in most computational aberration correction methods, and recently we proved fractal dimension has better performance in FF-OCT images [34].

The purpose of this work is to validate a quantitative 3D light scattering model from inhomogeneity and anisotropy tissue in full-field OCT, the fractal approach of which not only can indicate the subcellular-level morphological difference between benign and cancerous tumor lesions in early stage but also can be used as an image quality metric for digital aberration correction in the deeper region of the living sample. First, the proposed depth-resolved refocusing amount is compensated by measuring the contrast variation in the deeper region. The optimal fitting curve is measured by FF-OCT volumetric spectrum with conditions of fractal dimension convergence range. For comparison, the tissue-induced in-depth aberration was modeled by phase compensation. Second, after digital aberration correction of FF-OCT images, it enables extracting the temporal contrast that indicates the sample dynamics of the onion cell wall in mitosis and *ex vivo* mouse heart in delayed neuronal death.

2. Method

The microstructures of natural tissues can be described by fractal dimension only covering a limited range of length scales [35]. The *en face* images obtained with FF-OCT at micrometer-scale spatial resolution in three dimensions allow us to apply fractal analysis to details of tissue structures comparable to those seen with traditional histology. The refocusing compensation method is based on the estimation of inhomogeneous scales by fractal analysis and converging the fractal dimension throughout one volumetric FF-OCT data along the Z-axial direction.

2.1. Protocol of the volumetric FF-OCT signal

The volumetric FF-OCT data of *ex vivo* mouse organs were obtained with the home-built FF-OCT system in Ref. [36], but uses the improved Köhler illumination described in Ref. [34]. A 20 W tungsten halogen lamp provides uniform illumination with broad bandwidth. The central wavelength and spectral half-width of the light source are $550nm$ and $200nm$, respectively. The power incident on the sample ranges from one to a few milliwatts by adjusting the home-built field stop and aperture stop. An identical pair of water-immersed microscope objectives (UMPLFLN 20XW, Olympus) was used as imaging lenses in two arms. The axial and lateral resolution of the FF-OCT system are around $1.4\mu m$ and $0.8\mu m$. The interference from Linnik interferometry is integrated into the area-array camera (MV1-D1024E-160-CL, Photonfocus), which works at the rate of 150 frames/s. Each volumetric data consists of X-Y-Z coordinates (x, y, z) and a frame number(t), which can be expressed as $I(x, y, z, t)$. The standard FF-OCT volumetric measurements consisted of $1024 \times 1024 \times 200$ in pixel size, representing the field of view (FOV) of $800\mu m \times 800\mu m \times 200\mu m$ in the physical dimension. Four frames were acquired with four-phase shifting by PZT to obtain one standard *en face* FF-OCT image. The effective refresh rate of the system is 37.5 frames/s, and the volumetric acquisition time for standard FF-OCT was 5.3 s. For the tissue dynamics imaging, 1600 sequential *en face* frames are captured in 10.6 s at the same location in the sample. The Photonfocus CMOS sensor with a full well capacity (FWC) of 200 ke- is optimized for high dynamic range applications and a high signal-to-noise ratio (SNR). The data was transferred to a frame grabber (MicroEnable IV AD4-CL, Silicon Software) using the high-speed CameraLink. The external trigger of the frame grabber was synchronized with a pair of translation stages through a DAQ device (National Instrument). One of the translation stages is placed under the sample for Z-axis scanning during measurement, while the other one is placed under the reference mirror for finding the zero optical path difference in alignment. Each tomographic stack was demodulated and obtained from a home-built LabVIEW program.

2.2. Fourier spectrum analysis of FF-OCT signal in scattering medium

At the microscopic scale, e.g. FF-OCT images, tissue can be modeled as random continuous medium, and the properties of light scattered from random bulk media such as tissue are related to the spatial correlation of the fluctuations of the refractive index between any two points within a tissue. The approximate form of the correlation function of scattering potentials of stochastic media can be determined by measuring the cross-spectral density function of the scattered light. Fractal analysis extracts the ranges of the spatial frequency components of tissue scattering potential by fitting the spectrum of index inhomogeneities of en face tomographic images to the fractal model of the spatial correlation function of the tissue.

Suppose the sample is thick and consists of large-scale inhomogeneities immersed in a scattering medium made of randomly distributed scattering centers. The refractive index inhomogeneities with sizes on a continuum between inner scale l_0 and outer scale L_0 can be defined for modeling the scattering medium [37]. In addition, the partial coherence illumination-based FF-OCT signal is an integration over a broad spectral range, the exponential decay of signal with depth and the extinction length l_e can be used to describe the microscopic length scale of disordered scattering media and the thickness of sample [38]. Here, we have the relationship of scattering scales $l_0 < l_e < L_0$. For the terminology from atmospheric turbulence theory, by the classical Kolmogorov model, the inner length scale characterizes the microscopic random inhomogeneities in the sample, and the outer length scale characterizes large-scale deterministic fluctuations of the dielectric function. For biological tissue, as a first approximation, it is plausible to assume that the mean of the refractive index, the length scale of refractive index correlation distance, and its variance are approximately constant from normal to disease state. Therefore, in the proposed fractal-based FF-OCT model, L_0 is the limited range of length scale and is stable ranging from $1\mu m$ to $2\mu m$ by different NA (numerical aperture) of microscope objectives.

In the first-order single scattering paraxial approximation, the intensity attenuates exponentially. Then statistical averaging is taken over an ensemble of different realizations of the scattering medium by considering the refractive index of tissue as a random function of position. It has been deduced that the spectrum of the light at any point in the image plane is proportional to the Fourier spectrum of the refractive index correlation function of tissue [39]. By using a model resembling the classical Kolmogorov model of atmospheric turbulence, the Fourier spectrum of the refractive index correlation function $\Phi(\kappa, z = Z_0)$ can be expressed in radial coordinates as follows [40],

$$\Phi(\kappa, z = Z_0) = \frac{4\pi < \delta n^2 > L_0^2(m-1)}{(1+\kappa^2 L_0^2)^m} \tag{1}$$

where Z_0 indicates one specific position of each *en face* image that is parallel to the direction of light propagation, where the δn is the spatially varying part of the refractive index of biological tissue, L_0 is the outer scale to indicate the refractive index inhomogeneities, whereas l_0 is the inner scale, respectively. In Eq. (1), the values of exponent $m(z)$ determine the shape of the spatial correlation function of the refractive index, and the fractal dimension of a two-dimensional surface can be measured by using equation $f'(z) = 4 - m(z)$. This can be described mathematically by atmospheric turbulence, indicating the *en face* surface roughness of backscattering light demodulated by FF-OCT.

In each layer of the volumetric FF-OCT, the scattering function at any point with depth can be expressed by $S(\vec{r}, z)$ and it can be shown that [15],

$$\left\langle |S(\vec{r}, z = Z_0)|^2 \right\rangle = \frac{\pi^2}{\lambda^4} < n > \Phi(\kappa, z = Z_0) \tag{2}$$

where the κ is the spatial frequency, and the angle brackets denote the average value taken over the ensemble of different realizations of the scattering tissue. Please note when collecting data with a camera, the cartesian coordinate system was used, then we transformed intensity data to the polar coordinate system before doing radial Fourier transformation.

2.2.1. Fourier-fractal refocusing algorithm of FF-OCT

The flowchart of the proposed method is shown in Fig. 1. The input is three-dimensional volumetric data that has been processed by conventional FF-OCT. Two essential steps are training a Fractal model H1 and then building a defocusing correlation matrix D(Z) for each layer in Z-axis.

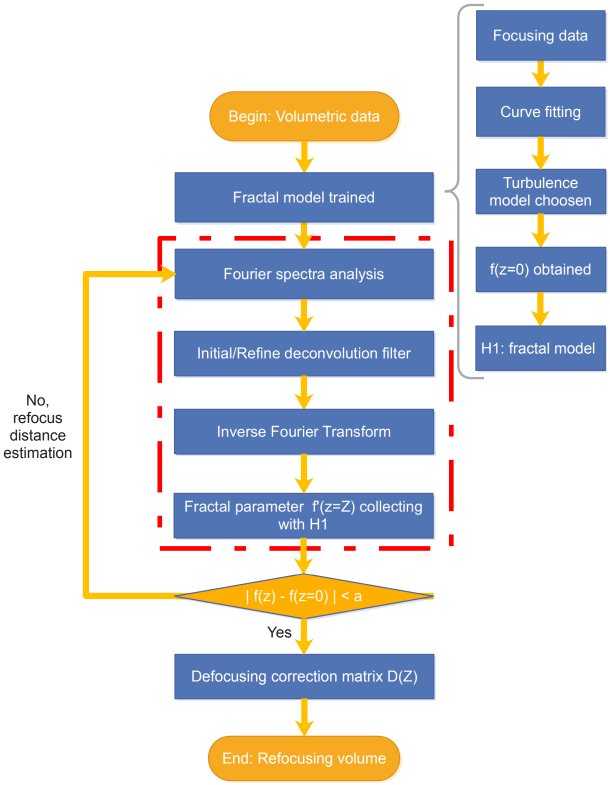
Focusing data
Curve fitting
Turbulence model choosen
f(z=0) obtained
H1: fractal model
Begin: Volumetric data
Fractal model trained
Fourier spectra analysis
Initial/Refine deconvolution filter
Inverse Fourier Transform
Fractal parameter f'(z=Z) collecting with H1
No, refocus distance estimation
| f(z) - f(z=0) | < a
Yes
Defocusing correction matrix D(Z)
End: Refocusing volume

Fig. 1. Flowchart of Fourier-fractal refocusing algorithm.

The fractal model H1 is trained from the obtained data in the focus plane. The power spectral density (PSD) of the index inhomogeneities in the focus plane of tissue will be obtained by radial Fourier transformation of volumetric data. To extract the spectrum of index fluctuations quantitatively, we fitted parameters m and length scale L to the Von Karman spectrum by Eq. (1). The value of the parameter m determines the shape of the spatial correlation function and is related to the fractal dimension of tissue. It can be approximately equal to one-half of the measured slope in the range of power-law scaling. Its magnitude is related to the fractal dimension of a two-dimensional surface. Then, the fractal dimension of tissue can be estimated by FracDim(Z) = 4-m(Z) [14,15]. Two different curve fitting methods were compared for determining the shape of the turbulence model by Von Karman spectrum with measured spectral data. The slope is firstly fitted according to an inverse power law function of depth Z in PSD fitting method. For simplified fitting processing, the slope is also fitted to a linear function of depth Z. Since the linear fitting method fits only for the linear part of the measured spectral data, the main advantage over the PSD fitting method is saving computing power. The cutoff spatial frequency of sampling pixels of camera resolution is set as the end of fitting boundary. We validated the the fitting methods by in-focus and out-of-focus data in the result part. Finally, the in-focus fractal model H1 of depth Z is trained for every single sample. Also, the fractal dimension model can be optimized by higher sampling density using more pixel resolution of image.

The defocusing amount of defocus data in the sample is estimated by the same step of parameter m and length scale L. Then we build an initial deconvolution filter and use inverse Fourier transform to reconstruct the refocusing volume. Then again, we calculated the fractal dimension of refocusing data and compared it with model H1; only in the condition of convergence enough to the ideal in-focus fractal model the defocusing correction matrix D(Z) can be built. Finally, the output refocusing volume is refocusing volume by multiplying input data by refocusing the correction matrix. The depth-dependent defocusing correction matrix $D^{'-1}(\rho, \delta z)$ in Fourier domain can be expressed as follows [39]:

$$D^{'-1}(\rho, \delta z) = exp(-i \cdot \frac{\lambda \delta z}{2\pi} \cdot \rho^2) \tag{3}$$

where ρ is the spatial frequency, and δz is refocused distance. The fractal parameter, $m(z = Z)$ or $f'(z = Z)$ (in Eq. (1) and Fig. 1), determines the shape of the spatial correlation function of the continuous random refractive index distribution, and it is also converging when scattering decay with depth [19]. The refocused volumetric structures $F(\vec{r}, z = Z0)$ can be expressed by Eq. (4):

$$F(\vec{r}, z = Z0) = \mathcal{F}^{-1}\{\ \mathcal{F}\{\ S(\vec{r}, z = Z_0)\}\ \times D^{'-1}(\rho, \delta z)\} \tag{4}$$

The defocus of each *en face* image can be quantitatively defined by fractal dimension and measured by the deviation values of the fractal parameters compared with in-focus data. For each *en face* tomographic image, we measured the change of contrast by fractal deviation values with/without the proposed defocus compensation. In the result section, Fig. 5(a) presents the fractal deviation values.

2.2.2. Fitting curve and trained fractal models of volume spectra

The selection of power spectral density curve fitting and linear curve fitting models are decided by fitting accuracy and temporal resolution. The power spectrum of index variations was fitted by radial Fourier transformation of the measured FF-OCT volume spectra with X axis of spatial frequency in the log-log scale.

The linear fitting model relies on a weighted least-square estimation of linear scaling of the logarithm power spectrum on specific spatial frequency to Eq. (1), while the second fitting method suggests a power-law scaling that contributes to index variations in this range. The linear fitting method neglects some of the power spectrum density that near-zero frequency and may have a higher accuracy of slope measurement in experiments than the power-law method.

The trained fractal model H1 will be employed for phase correction in the following step in Fig. 1.

2.2.3. Fractal dimension convergence range

Fourier spectrum analysis of the FF-OCT signal indicates the propagation of not only interference but also the fractal dimension.

The ground truth of normal and abnormal or even cancerous samples is observed and diagnosed by clinicians. In fractal theory, the normal tissue has more evenly distributed, or scatterers are distributed randomly that are not changeable. Then we experimentally measured the fractal tissue parameters in previous work, of which the data showed a stable fractal dimension trend between 2.4 to 3.64 accordingly [34,41,42].

In the flowchart in Fig. 1, a is a constant to converge fractal parameters in depth. Then a summary of experimentally measured fractal tissue parameters was added to enrich the database for human organs.

2.3. In-depth tissue-induced aberration in FF-OCT

Tissue-induced aberration includes spherical, dispersion, and defocus effects in FF-OCT. As is shown in Fig. 2, the light rays bend when it propagates from medium to tissue, and object A on the back focal plane of the objective will be imaged as A'' due to Snell's law. However, the ideal image should be A' without refraction mismatch. The focal and coherent planes will be separated, and this is the defocusing in FF-OCT. In this case, the image contrast in FF-OCT decreases with the increase of the axial separation of the centers of the spatial coherence envelope and the temporal coherence envelope due to the defocusing effect [19]. Normally, the change of contrast with the defocus can be calculated by estimating the optical phase with/without refractive index mismatch in the light field backscattered from the sample. It is necessary to calculate a refocus distance in the reference arm for matching the coherence plane with the new focus position for each step scanning in depth [20,21,23]. The computational refocusing compensation proposed in this work is not only mechanics-free but also independent of the operator during acquisition and processing. However, another issue needs to be fixed when using fractal-based refocusing compensation. The differences between the microscopic structures and the ones observed in the FF-OCT image should be separated by comparing the tissue-induced decrease with the variations due to the local refractive index, which phase changes can model. The phase difference of tomographic image interference signal can be expressed as,

$$\Phi(z) = \Phi_0(z) + \Phi_{sph}(z) + \Phi_{dis}(z) \tag{5}$$

where $\Phi_0(z)$ represents the phase difference between the two interference arms when the microscope objective is ideally focused on a specific layer of the biological tissue sample, the $\Phi_{sph}(z)$ represents the additional phase caused by spherical aberration and the $\Phi_{dis}(z)$ represents the additional phase caused by chromatic aberration. In the case of tissue-induced aberration, the biological sample is assumed to be a homogeneous and isotropic medium in low-order aberration situations. For example, low-order spherical aberration is caused by the mismatch between the average refractive index of the biological tissue sample and surrounding medium and high-order spherical aberration is caused by inhomogeneity of the refractive index distribution within the biological tissue sample. In general, the effect of low-order spherical aberration on the image quality is higher than that of high-order spherical aberration. Moreover, the structure of biological tissues is complex, and the refractive index distribution cannot be determined by conventional methods. In the case of a real biological sample, the elimination of high-order aberration may be one limitation. But fractal analysis can deal with this case because in the fractal model, we consider the tissue contains refractive index inhomogeneities or variations with sizes on a continuum range. More simulations and experiments are ongoing.

The spherical compensation has been proposed by analyzing the optical path with the medium and tissue refraction index. The compensation phase can be expressed as [43],

$$\phi_{sph} = \int_0^1 2\kappa(l'_{ide}\sqrt[2]{n_t^2 - (NA\rho)^2} - l'_{act}\sqrt[2]{n_m^2 - (NA\rho)^2})d\rho \tag{6}$$

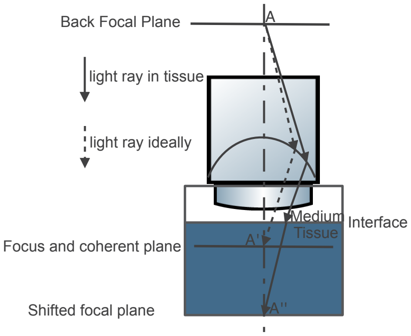

Fig. 2. Ray tracing model for defocus and spherical aberration.

where ρ is normalized numerical aperture, κ is the wavenumber, n_t and n_m is the tissue refractive index of its surrounding medium, respectively. l'_{ide} and l'_{act} represent the distance that light ray travels directly in medium and bend in tissue, respectively.

FF-OCT systems use a low-coherence white light source, which has a broad spectral width and causes chromatic aberration. Since the light passes through the inside of the tissue twice, the additional phase difference $\Phi_{dis}(z)$ can be expressed as:

$$\phi(\Omega) = 2\kappa(\Omega) l'_{act} \tag{7}$$

where $\kappa(\Omega)$ is the function of the difference of angular frequency, ω is center angular frequency, the Taylor expansion of $\phi(\Omega)$ can be expressed as [44],

$$\phi(\Omega) = [2\kappa(0) + 2\kappa^1(0)\Omega + 2\kappa^2(0)\Omega^2/2 + 2\kappa^3(0)\Omega^3/6 + \cdots] l'_{act} \tag{8}$$

where as the $\kappa^n(0) = \frac{d^n\kappa}{d\omega^n}$. The second-order and third-order dispersion can be cauculated by:

$$\kappa^2(0) = \frac{\lambda^3}{2\pi c^2}\frac{d^2n}{d\lambda^2} \tag{9}$$

$$\kappa^3(0) = -\frac{\lambda^4}{4\pi^2 c^3}\left(3\frac{d^2n}{d\lambda^2} + \lambda\frac{d^3n}{d\lambda^3}\right) \tag{10}$$

thus, the additional phase introduced by dispersion can be deducted as follows,

$$\Phi_{dis} = 2\pi\lambda_0^3 l'_{act}\left(\frac{d^2n}{d\lambda^2}\right)|_{\lambda_0}\left(\frac{1}{\lambda} - \frac{1}{\lambda_0}\right)^2 - 2\pi\lambda_0^4 l'_{act}\left(3\frac{d^2n}{d\lambda^2} + \lambda\frac{d^3n}{d\lambda^3}\right)|_{\lambda_0}\left(\frac{1}{\lambda} - \frac{1}{\lambda_0}\right)^2 \tag{11}$$

$$\phi_{dis} = \int_{0.45}^{0.65} \Phi_{dis} d\lambda \tag{12}$$

where the $\lambda_0 = 0.55\mu m$, $\Delta\lambda = 0.2\mu m$, for the convenience of calculation, it is assumed that the biological tissue sample and the immersion medium are uniform and isotropic, and the interface between the two media is horizontal and perpendicular to the optical axis. Besides, additional optical phase differences due to the second-order and third-order dispersion were measured using the refractive index of water for simplification, then the relationship of refractive index with wavelength is [44,45]:

$$n(\lambda) = 1.3231 + \frac{3.3 \times 10^{-3}}{\lambda_2} - \frac{3.2 \times 10^{-5}}{\lambda^4} \tag{13}$$

In the result part, we used Matlab to calculate the contrast per pixel and then compared *en face* tomographic images of the fresh liver with and without aberration compensation. In the comparison study, Matlab with contrast per pixel was used to measure the quality of the image contrast, and it is defined as the average intensity difference between a pixel and its adjacent pixel.

2.4. Temporal-contrast enhancement in volumetric FF-OCT signal

Dynamic activities can be extracted by recording a movie of volumetric FF-OCT signal, which was first introduced by Ref. [46] with the term dynamic full-field optical coherence tomography (dFFOCT). The difference from conventional FF-OCT is the phase difference between a sample and reference arm changes with the absolute movement by single scatter or relative motion between scatters. The dynamic signals are less sensitive to amplitude changes than phase changes for absolute movement by one single scatter or bulk scatterers. The scatterer's size and refractive index are stable for one region of interest (ROI) in the sample. Therefore, the number of scatterers in ROI changes only when scatters leave the ROI or when new scatterers enter the ROI, thus affecting the amplitude $\alpha(x, y)$ of the interference signal. If the scatterers are in uniform linear motion in the axial direction, it results in a sinusoidal signal I of amplitude and phase signal. The scatterer must move from one region to its neighbors to cause intensity change. The transverse range is about half of the system's lateral resolution(about $500nm$). The phase affects the spatial distribution of scatterers. The scatterers move axially about a quarter of a wavelength(about $100nm$), and then the intensity I is able to reach a maximum. Therefore, in dynamic signals, the axial displacement contributes more than the transverse displacement of scatterers.

In dFFOCT, there is no reference modulation, and only movements in the sample contribute to the signal modulation. Therefore, the interference signal I detected by the camera can be expressed as [46]:

$$I(x, y, t) = I_0(x, y) + \alpha(x, y)cos(\frac{2\pi}{\lambda}(\Delta(t) + \delta(t))) \tag{14}$$

Where $I_0(x, y)$ is background intensity at a given pixel (x, y) and t is for time, $\alpha(x, y)$ is amplitude, $\Delta(t)$ is the phase changes induced by bulk motion (static scatters) in the axial direction, while $\delta(t)$ indicates the relative motion (metabolic scatters) between scatters in tissue. Usually, bulk motion is slower than relative motion. For living tissue imaging that uses the ultra-high-speed camera, if the framerate is faster than the change of bulk motion while slower than the change of relative motion, the relative motion effect can be neglected so that bulk motion is dominant. However, if the framerate is faster than the change of relative motion, more rapid dynamic information can be observed.

The dynamic signal is computed as the average of the running temporal standard deviation. First, acquire the raw movie from $I(x, y, t)$; second, cut the movie into sub-movies; then remove motion artifacts by singular value decomposition (SVD, as an adaptive filter that could separate motility signals from motion-induced signals), as $S(x, y, t_i)$ and compute the mean value $\langle S(x, y)\rangle$ for each sub-movie; Finally, compute the standard deviation for each sub-movie [47]. For the tissue dynamics imaging measurement protocol, 1600 sequential *en face* frames are captured in 10.6 s at the same location in the sample. Therefore, the processed dynamic signal can be written as $D(x, y)$ [46]:

$$D(x, y) = \langle\sqrt{\frac{1}{N}\sum_{i=1}^{N}(S(x, y, t_i) - \langle S(x, y)\rangle)^2}\rangle \tag{15}$$

where D(x,y) is the dFFOCT signal at a given pixel (x, y) and t_i means time at the index of number N. The mean value of the standard deviation was calculated on several sub-stacks N of the raw movie I. All dFFOCT images or values are computed from a movie of 1600 images with sub-stacks of 40 images, then the four results images are averaged to give the final dFFOCT image. The dynamic signal was obtained by subtracting the next frame from the previous one, and the sliding window of the signal running STD (Standard deviation) is N=40.

To extract the motion pattern, the Fourier transform was used from the time axis. The time spectral imaging visualized the active region of both bulk and local motion by mapping dFFOCT signal to HSV (Hue, Saturation, Value) color space [3]. Due to the limit of computational efficiency by convention matrix decomposition filtering, adaptive filtering was proposed in this work to suppress the motion artifacts in that the long-term observation of time-lapse imaging is coded only by Hue. The idea is that the first color image was used as a template and converted from RGB color to HSV color space. The value of the first Hue channel was then used as a calibrated mask, and the remaining dFFOCT images used the mask to convert for color stabilization during time-lapse imaging [48]. For the temporal-contrast enhancement in volumetric FF-OCT signal, the possible instabilities are moving the translation stage, camera, and tissue degeneration under long-term exposure to the illumination. When triggers the moving stage under sample, we set a time gap for acquisition. After acquiring the volumetric data, the first step is to correct the camera frame-to-frame instability by normalizing each frame to compensate for exposure time variations. We keep adding solutions to the sample and keep the total measurement time for each sample under several minutes.

3. Mouse organ evauation

3.1. Sample preparation

In this study, we imaged various organs procured from freshly euthanized mice, utilizing a protocol approved by the Wuxi Third People's Hospital Committee. Seven organs, including the esophagus, small intestine, spleen, kidney, liver, intestine, heart, immediately after carbon dioxide-induced euthanasia. Each of these organs was collected for immediate *ex vivo* imaging.

3.2. Study protocols

Two studies involving seven fresh mouse organs imaging with FF-OCT were performed to evaluate the proposed fractal-based refocusing method and visualize the high active distribution of scatters in tissue.

Study 1 involves observation of image contrast to validate refocusing distance in fresh liver tissue through measurement of fractal dimension curve. The first hypothesis is that the surface is the most robust for one volumetric tissue data. The second hypothesis is that for one volumetric tissue data, the bottom fractal parameter is slightly normal with the surface fractal model. The last one is for one volumetric tissue data, though the fractal parameter in the bottom layer is abnormal, but sub-group of fractal parameter is still convergence to the surface ones. Besides, study 1 also involves a cross-sectional investigation of multiple fresh organs to build an experimentally measured fractal tissue parameters library, which was performed to validate the utility of the fractal analysis as a method for image contrast evaluation.

Study 2 compensates for depth-resolved optical aberration compensations and explores dynamic contrast fused with the FF-OCT signal. For one dynamic FF-OCT image, a cube of $1024 \times 1024 \times 1600$ direct FF-OCT interference was acquired as a movie of 1600 images consisting of 400 images after four averaged images. The dynamic signal was obtained by subtracting the next frame from the previous one, and the sliding window of the signal running STD (Standard deviation) is 40. The minimum frequency 2Hz was considered in the Fourier domain. We set this spatial frequency as the smallest index of normalized PSD (Power spectral density) of raw data. It is not directly related to moving window size but must be smaller than the number of sliding windows after averaging.

In addition, please note that the mouse was sacrificed, and fresh organs (liver, spleen, kidney, heart, lungs, small intestine, and esophagus) were collected for immediate *ex vivo* imaging. We observed that the heart was still beating for a pretty long time (around 30 minutes). We did some literature research and also asked the doctors and operators if one of the possible reasons is the attenuation of delayed neuronal death [49].

4. Results

4.1. Histology-like images of fresh mouse organs

In this study, we imaged fresh(unfixed, unsanctioned, unstained) *ex vivo* tissues from seven different mouse organs, including the esophagus, heart, intestine, kidney, liver, small intestine, and spleen. The goal was to recapitulate the normal histology of these organs by identifying various tissue microstructures [50]. We regard section-based histology images as the golden standard, and we compared the tomographic images with histology images with the help of clinicians and operators from the Hospital.

Figure 3 shows tomographic images obtained from *en face* of the esophagus, small intestine, spleen, kidney, liver, intestine, heart, and onion root tips that were undergoing mitosis with a home-built FF-OCT system. The thickness of one *en face* slice is 1 μm and the thickness of each tissue sample of mouse organs is around 1 cm. In Fig. 3(g) and Fig. 3(h), two images obtained by axial scanning of heart tissue. The contrast in Fig. 3(g) comes from the ventricular chamber. In contrast, in Fig. 3(h), the signal decayed at a depth of 100 μm due to the imaging penetration limit of the visible band wavelength in the light source. We imaged all mouse organs simultaneously. Some contrasts are relatively low, and some structures are not resolvable should be due to tissue-induced aberrations, interfacial reflections, or scattering from various overlying tissue elements.

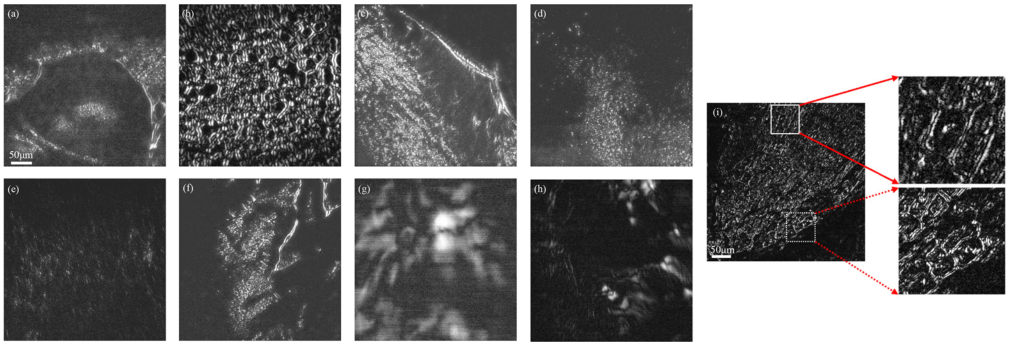

Fig. 3. *En face* histology-like tomographic images of (a) Esphagus; (b) Small intestine; (c) Spleen; (d) Kidney; (e) Liver; (f) Intestine; (g), (h) Heart at different depth; (i) Onion root tips undergoing mitosis.

4.2. In-depth fractal dimension curve observation and analysis

For choosing the optimal model for refocusing distance measurements in each fresh organ, Study 1 involved fractal dimension curve fitting and refocusing distance compensation in fresh mouse tissue. The fractal dimension model with its optimization and the fractal dimension curves measurement method can be accessed in Section 2.2.1. The result of in-depth fractal dimension curves is given in Fig. 4. Each pixel in depth has an interval of 1μm.

Figure 4(a) compares the fractal dimension curve by fitting the linear model with the power spectra density (PSD) model in the mouse small intestine. Both models can be accessed in Section 2.2.1 in Method. The fitting model based on power spectra density has a flat fluctuation of the fitting curve in-depth. Since in PSD fitting, all the data is used not only in the background, but the flat fluctuation of the fitting curve strongly indicates the turbulence model parameter m, and scale length does not change with depth in tissue. The calculation of the turbulence model can be accessed in Section 2.1.1 of Method. If the flat fitting curve occurs in PSD fitting, the turbulence model cannot show the refractive inhomogeneous in this tissue. Moreover, it also

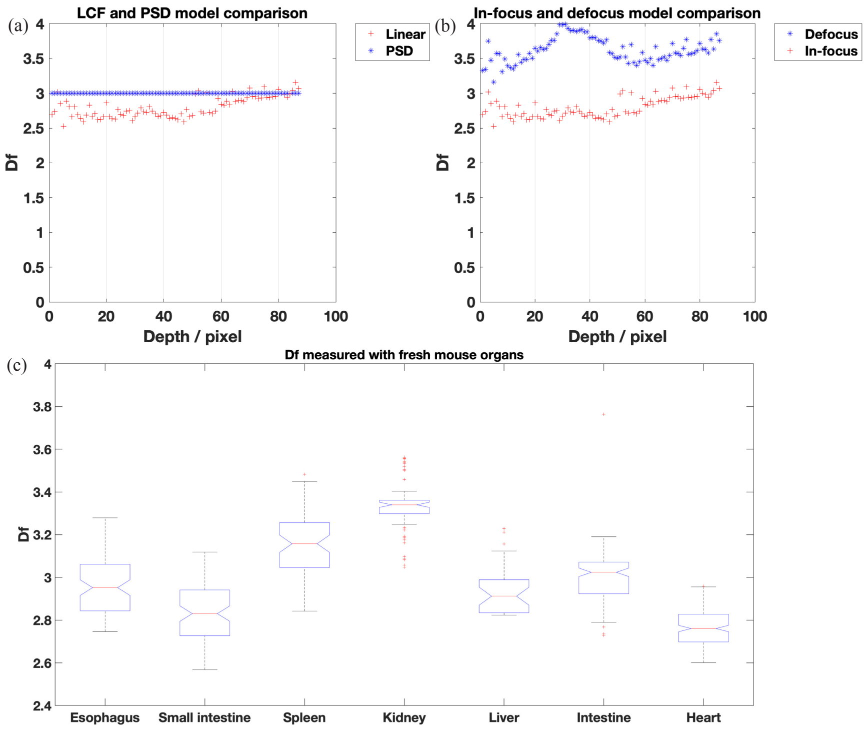

Fig. 4. (a) The D_f compares linear with PSD curve fitting model in same tissue from Small intestine; (b) The D_f compares in-focus with out-of-focus data in same tissue from small intestine; (c) The boxplot of refocused D_f in seven mouse organs.

suggested that the background signal may affect the PSD fitting method more than the linear model. Thus, we use the simplified linear fitting method instead.

In Section 3.2 Study protocols, Study 1 suggests the fractal model trained with in-focus surface data is the most robust for the volumetric aberration correction. Then, the volumetric data obtained from the FF-OCT system is used to generate the trained fractal model, of which the step has been shown in Fig. 1. As a result, Fig. 4(b) compares the linear fitting curve with in-focus and out-of-focus data obtained from the same sample. In-focus data is obtained from the surface of the tissue to the imaging depth of 87 μm, and the out-of-focus data was obtained at 20 μm defocus distance from the in-focus data. For the out-of-focus thin layer of the mouse organ, the blue asterisks curve in Fig. 4(b) shows that the fractal dimension D_f generated by defocus data has higher variations than in-focus data marked with the red cross. It validated that the in-focus trained fractal model can compensate for volumetric data. In addition, it also can be summarized from Fig. 4(b) that the convergence range of defocus data trained fractal model is generally higher than the in-focus trained fractal model.

Therefore, we measured seven D_f curves of mouse organs by choosing infocus data with a linear fitting strategy. The refocused D_f boxplots of each organ were drawn in Fig. 4(c). The convergence range is somewhat between 2.5 to 3.8.

As is shown in Fig. 5, we compared the cross-section in the axial direction obtained from mouse liver tissue to validate the effect of refocusing compensation. In the figure legend of Fig. 5(a), the blue asterisk and black box show fractal dimension changes with physical depth in sample tissue before and after refocusing correction with the trained fractal model, respectively.

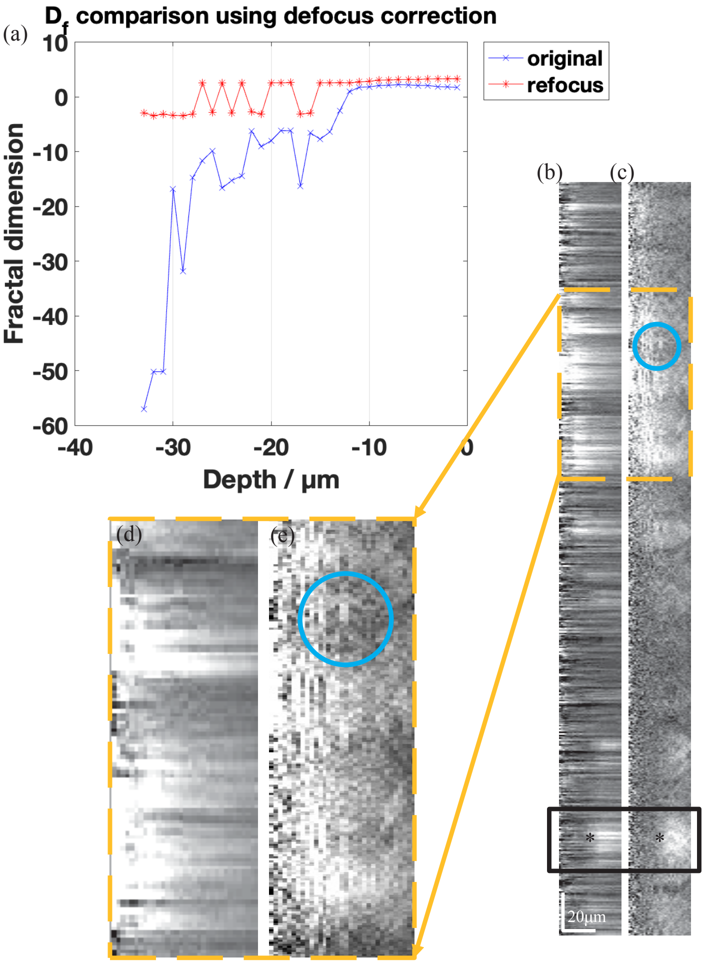

Fig. 5. (a) In-depth fractal dimension curve comparison; (b),(c) FF-OCT images of fresh mouse liver tissue without and with applying refocusing, respectively.

Figure 5(a) observes that the fractal dimension curve firmly drops when signals go deep down in liver tissue. In the figure legend of Fig. 5(a), the blue asterisk and black box show fractal dimension changes with physical imaging depth in sample tissue before and after refocusing correction with the trained fractal model, respectively. The y-axis indicated that the fractal dimension without refocusing correction ranged from −60 to 4 (not 10) in Fig. 5(a). First, in the deeper tissue region, it suggested that defocus, multiple scattering signals, and higher order interact aberration strongly affect the fractal dimension. Second, it can be corrected to range from 2.5 to 3.8. Thus, the fractal dimension is valid for a minimum depth range of about 10-15 μm, and all imaging depth is marked with the red cross after defocusing compensation by the proposed method. Furthermore, Fig. 5(a) validated the hypothesis for one volumetric tissue data. However, the fractal parameter in the bottom layer is abnormal, a sub-group of fractal parameter convergence to the fractal dimension in the surface after refocusing. The red line in Fig. 5(a) expresses D_f curve after refocusing compensation, of which the curve is convergence. However, the below line marked with a blue dash showed unclear Fractal dimension when depth is from $35\mu m$ to $15\mu m$.

Figure 5(b) and (c) compared the same X-Z cross-section images extracted from mouse liver tissue samples with/without fractal-based refocusing. In the area marked with the black square with asterisks in Fig. 5(b), by refocusing algorithm, the same region is stronger scattering-like signals in the deeper region (from left to right) in Fig. 5(c). In the box region of Fig. 5(b) and (c) (magnified in Fig. 5(d) and (e)), we can see the overexposure pixels in Fig. 5(d) becomes evenly distributed and shows the property of homogeneous in the lateral direction. Please note that the minor stripe-like signals in the horizontal of Fig. 5(b) are mainly caused by sample motion and several aberrations (defocus, tissue-induced dispersion). The tissue motion comes from the moving transition stage under fresh mouse liver sample. Thus, the bulk sample motion in the axial direction can be reduced extraordinarily after fractal dimension-based refocusing compensation. As a result, compared with Fig. 5(d), the unresolvable signal in the same region shows higher contrast in Fig. 5(e). Moreover, the diameter and the shape in the blue circle marked area in Fig. 5(e) may be a hepatocyte with different homogeneity nearby rather than a speckle fluctuation caused by global axial motion. Please note that the *en face* images of fresh mouse liver tissue without and with applying refocusing can also be available in Fig. 7(a) and Fig. 7(c).

Therefore, it enhanced the image contrast in cross-sections in FF-OCT imaging and possibly indicated the distribution of tissues with different properties in axial and lateral directions.

Volume-based FF-OCT imaging of *ex vivo* mouse heart tissue at the same section slice was present in Fig. 6(a) and Fig. 6(b) in cross-sectional(X-Z) and longitudinal(Y-Z) direction. The physical size of this FF-OCT signal volume was $750 \times 750 \times 187 \mu m^3$ (XYZ).

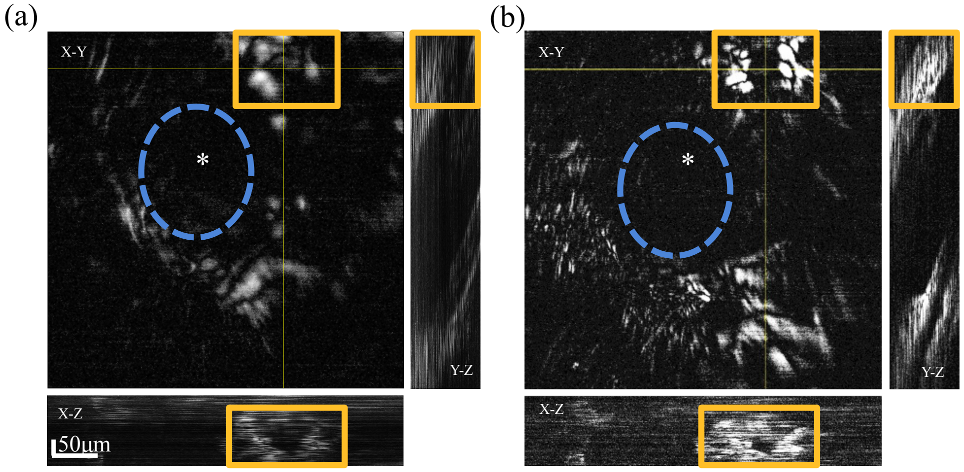

Fig. 6. (a), (b) Volume-based FF-OCT sectioned images of mouse heart without and with refocusing compensation.

The *en face* tomographic images shows less signal inside the blue circle, implying no signal from the empty chamber. The function of the ventricular chamber is to collect and expel blood towards the peripheral beds. The morphological structure of the ventricular chamber is the hollow spaces within the heart. In the FF-OCT modality, the backscattering signals are measured by interference with the reference mirror because the time delay is shorter than the light source coherence length. Although the structures of the ventricular chamber marked with the blue circle can neither be seen in a) nor b), in the yellow square, the cross-section images present the empty chamber's outer shape. In addition, the diameter of the empty area in the blue circle is around 300 µm, which has been observed in Ref. [50]. That is to say, the observed structure is the empty structure.

The white striated structures shown in Fig. 6(a) also consist of branching cardiac muscle fibers called myocardium. It can be seen from the solid yellow square that the stripe-like signal moved in the same direction in the X-Z and Y-Z cross-sections of Fig. 6(a) and (b), implying the longitudinal contrast is decreased due to not only the sample motion but also the heart beating. It can be seen from Fig. 6(a) and (b) that the longitudinal contrast is enhanced after the fractal-based refocusing algorithm, even though the attenuation of delayed neuronal death cannot be quantitatively measured in our lab currently. The refocused images are shown in Fig. 6(b), and cross-sections can observe the obvious enhanced contrast in X-Z and Y-Z directions.

In the region of the yellow square with a light yellow cross line at the center in Fig. 6, the *en face* and X-Z cross-section view displayed a spheroid-shaped chamber in which a black hole can be observed clearly. The Y-Z longitudinal-section view displayed the lateral branching muscle fibers of the myocardium. Therefore, the spheroid-shaped chamber is visible only in the 3D representation of the refocused volume.

As mentioned in Fig.4(c), we suggested that the convergence range of refractive index turbulence affects tissue heterogeneity with the proposed fractal model. The measured convergence range for fresh mouse organs is shown in Table 1, and the result indicated high consistency with the measured results proposed in Ref. [51]. Only when the tissue elements have sizes larger than outer scale L_0 can they be accurately described as randomly distributed [14]. In this work, the scale range can be determined by lateral resolution. As shown in Fig. 5 of Ref. [36], the edge response of the resolution target test chart indicates the length scale ranges is from $0.8\mu m$ to $1.7\mu m$.

Table 1. Summary of Experimentally Measured Fractal Tissue Parameters

Tissue Type	Fractal Dimension D_f	Scale Range (μm)
Esphagus	2.75-3.28	0.8-1.7
Small intestine	2.57-3.12	0.8-1.7
Spleen	2.84-3.48	0.8-1.7
Kidney	3.05-3.56	0.8-1.7
Liver	2.82-3.23	0.8-1.7
Intestine	2.73-3.76	0.8-1.7
Heart	2.60-2.96	0.8-1.7

We imaged the fixed heart tissue and presented them in Fig. 3(g) and Fig. 3(h), of which the imaging depth is at the surface and a depth of 100 µm. Then we found that horizontal lines appear almost everywhere in Fig. 3(g), and Fig. 3(h) shows some delicate structures, and the horizontal lines disappear in the deeper region. Due to the delayed neuronal death, we observed the beating issue when measuring *ex vivo* mouse heart tissue. This finding suggests dynamic microstructures need to be resolved by separating the heart beating with moving artifacts induced microstructures.

4.3. Tissue-induced contrast in FF-OCT

The tissue-induced aberrations were estimated and compared with the proposed fractal-based defocusing compensation method to demonstrate the enhancement after refocusing. Figure 7 compares reconstructed tomographic images after tissue-induced refocusing compensation with fractal-refocusing compensation in the same depth of fresh liver tissue. Figure 7(a) is *en face* tomographic images obtained from standard FF-OCT. Figure 7(b) is the corrected image with only tissue-induced aberration compensation. Figure 7(c) is the corrected image with only fractal-based phase compensation. These images are not processed with additional image processing but only with tissue-induced aberration compensation in the time domain and fractal-based phase compensation in the Fourier domain.

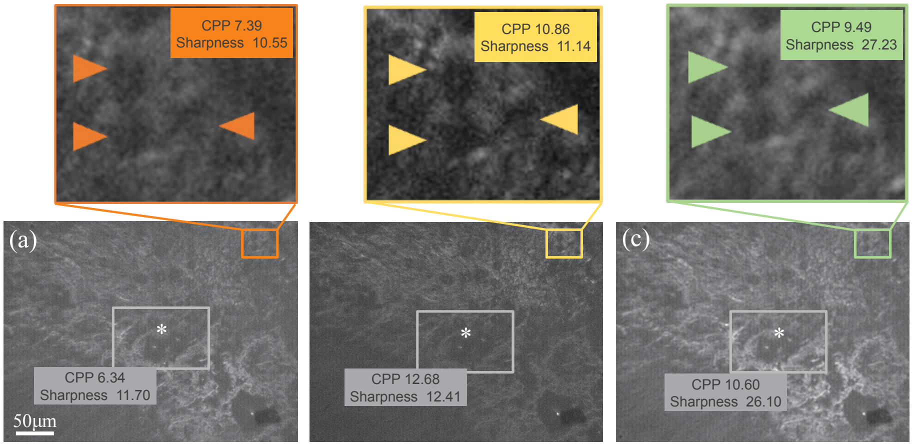

Fig. 7. *En face* tomographic images of fresh liver tissue (a) with amplitude reconstructions; (b) with tissue-induced aberration compensation; (c) with Fractal-based refocusing compensation

From the global viewpoint in Fig. 7, the brightness in Fig. 7(b) is lower than the other two because of time-domain image processing, and it looks the full brightness and contrast is decreased more. Figure 7(c) is an image processing in Fourier domain processing, of which the smaller spatial frequency components look mild.

Contrast per pixel and sharpness have been calculated to quantify the image quality in the bright and dark local areas. Contrast per pixel(cpp) is the average intensity difference between a pixel and its adjacent pixel. Sharpness uses the gradient magnitude sum of all gradient numbers of pixels to give us the sharpness metric. In the grey box area that displays the local bright region, the cpp in Fig. 7(a), 7(b), and 7(c) is 6.34, 12.68, and 10.60. The sharpness of the local bright region of Fig. 7(a), 7(b), and 7(c) is 11.70, 12.41, and 26.20. In the enlarged box area that displays the local dark region, the cpp in Fig. 7(a), 7(b), and 7(c) is 7.39, 10.86, and 9.49. The sharpness of the local bright region of Fig. 7(a), 7(b), and 7(c) is 10.55, 11.14, and 27.32.

It can be found from the result that the contrast and sharpness trend in both dark and bright areas is similar, and the amplitude reconstruction in Fig. 7(a) shows the lowest image quality in contrast and sharpness. Second, Fig. 7(b) shows better contrast per pixel in both dark and bright areas, and Fig. 7(c) shows better sharpness. Combined with the global viewpoint result, it may suggest that tissue-induced aberration correction obtains higher contrast than fractal-based phase compensation. However, it sacrifices the original intensity that looks to decrease the contrast. It also implies that the fractal-based phase compensation method shows more high-frequency details in the image while maintaining the original intensity.

Lastly, as the imaging depth increases to $30\mu m$, the effect of phase compensation becomes more evident. It can also be found that diseased organs may exhibit either uniform (or nearly uniform) refractive or significantly non-uniform properties. The diseased organ has many types, including precancerous, early, or late cancerous organs at different diseased stages. The local region may have a combined distribution of uniform or non-uniform properties in the refractive index. Thus, it is rational that the refractive index of cancerous tissues is higher than that of the normal tissue.

4.4. Fractal based temporal-contrast in FF-OCT

Figure 8(a.13)– 8(a.16) displayed FF-OCT *en face* images of the top four layers of the onion, while Fig. 8(c.56)– 8(c.59) presents the bottom four layers from the same sample. The thickness of one layer of the onion is $1\mu m$. For a volume data of $1024 \times 1024 \times 1600$ in x-y-z, the volume acquisition time is 10.6 s, and the distance between the first surface and the last bottom layer is around $200\mu m$. As is shown in Fig. 8(a), we observed the structures of flying micro bugs during onion cell mitosis. While at the bottom of the onion sample in Fig. 8(c), the flying micro bugs disappeared. It means that as the dynamic scatterers, the micro bugs leave the coherence section of the onion sample. In this study, we regarded flying micro bugs as a part of the onion sample, which will not interact with the onion. However, it can compare the dynamic differences between flying micro bugs and bulk onion cells.

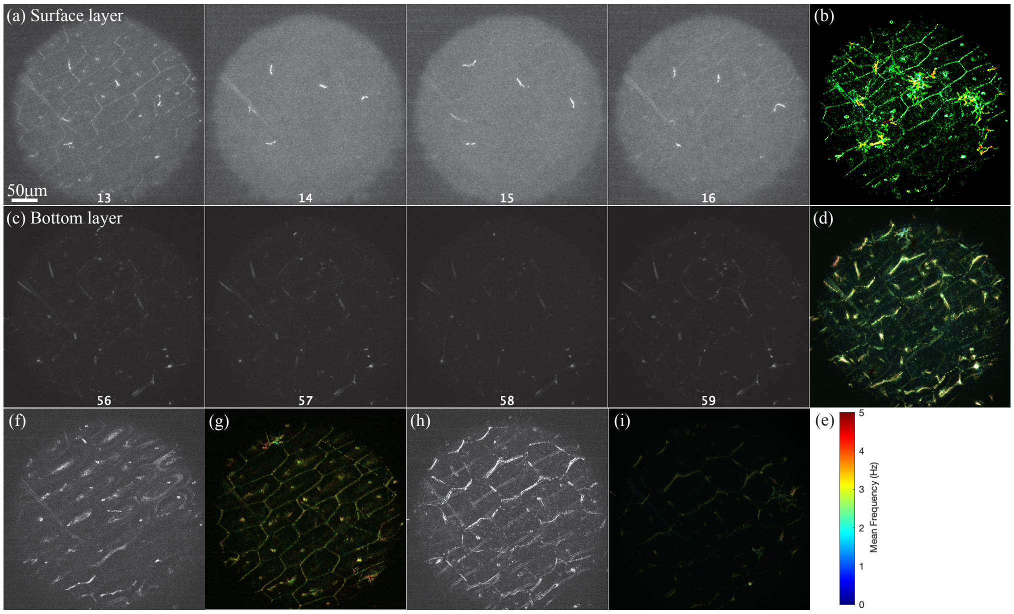

Fig. 8. (a),(c) *En face* tomographic images of onion with the interval time of 1ms; (b),(d) Temporal contrast of corresponding FF-OCT images; (e) Colour bar of mean frequency for temporal contrast; (f),(h) *En face* tomographic images of the semi-dehydrated and the utterly dehydrated onion sample; (g),(i) Temporal contrast from the same ROI in the semi-dehydrated and utterly dehydrated onion sample.

The intensity of temporal contrast shown in Fig. 8(b) and 8(d) comes from the STD of consecutive images from the same onion, and the color bar represents mean frequency as shown in Fig. 8(e). Figure 8(b) shows the temporal contrast obtained from an onion sample immersed in water and growing up from mitosis. The whole onion cell and flying micro bugs can be seen. Higher mean frequency denoted the flying micro bugs and green component indicate the slow activities of the whole onion sample. Figure 8(d) shows the temporal contrast from the bottom area of the same onion sample. The bottom images show the contrast of the onion cell wall. In the upper left corner of Fig. 8(d), the red and high mean frequency area may be the dynamic contrast of cell wall changes.

To exclude environmental vibration factors and validate the dynamic contrast from the onion sample, we also measured the temporal contrast of the same onion sample in the same environment during natural dehydration. It took 8 hours to become semi-dehydrating and 24 hours to completely dry and dead. Figure 8(f) and 8(h) showed FF-OCT images of the semi-dehydrated and the utterly dehydrated onion from the sample. The former showed water-like cytoplasm in the onion cells and a few dot-like nuclei, while the utterly dehydrated clearly can hardly see contents in cells but only show the cell wall. Figure 8(g) and 8(i) showed temporal contrast from the same ROI in the semi-dehydrated and utterly dehydrated onion sample. Figure 8(b), 8(g), and 8(i) showed the gradual disappearance of dynamic signals of the cell wall. Figure 8(i) nearly showed very few dynamic signals in the dehydrated onion sample, which may be considered environmental vibration. There are two deductions. On the one hand, the dead cell of the completely dehydrated onion sample is static, and flying micro bugs are almost dead, so there is no dynamic signal; on the other hand, the environment vibration did not affect the dynamic contrast that much. So, it may suggest that the possible dynamic difference comes from contents in onion nuclei and cell wall changes, which come from the sample itself.

Therefore, label-free fractal-based temporal-contrast modality shows subcellular resolution recording of dynamic scatters of the growing-up cell wall and some micro activities. However, the different degrees of cell viability still need to be conducted in future studies.

Figure 9 shows the proposed Fractal-based contrast augmented FF-OCT images for fresh tissue imaging. In the center of the red triangle region of image a1, a3, a5, and a8, white roof-like structures show the periodic beating near the heart chambers. It may relate to heart beating rhythm. The yellow circle in image a2, a6, and a7 indicate the chamber area, of which the structures' appearances and disappearances in the chamber may suggest remaining blood transmission due to delayed neuronal death. In the blue triangle of image a1, a4 and a5, the dense distribution of strip-shape in the heart shows branching muscle fibers of the myocardium. Cardiac muscle fibers possess many mitochondria and myoglobin. The contractions of heartbeats are controlled by specialized cardiac muscle cells called pacemaker cells that directly control heart rate. These can be seen in Fig. 9(b) by color displayed in frequency. The mean frequency measured in Fig. 9(b) has a stable range from 0 to 5Hz according to seven types of mouse organs. Blue indicates the area of inactivity in cells or a deep microvascular layer, while the red zone can be heartbeat-related metabolic activities.

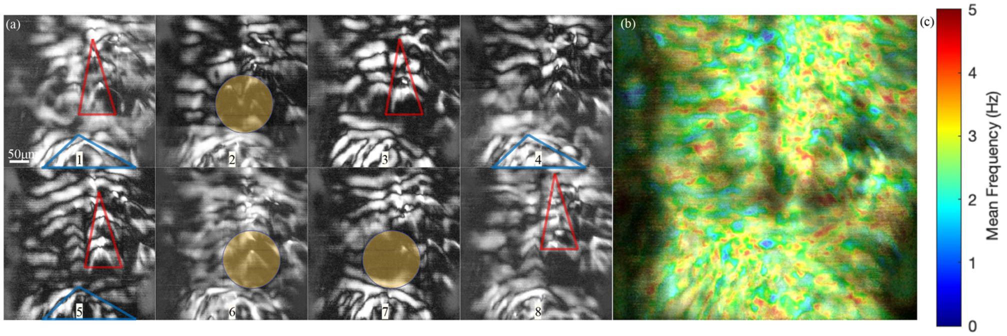

Fig. 9. Contrast-augmented FF-OCT images. (a) A series of FF-OCT images of fresh heart tissue; (b) Contrast augmented FF-OCT images of fresh heart tissue; (c) Colorbar of contrast augmented FF-OCT images.

In heart tissue imaging, the relative motion comes from cardiac muscle fibers and the ventricular chamber when the heart is still beating due to delayed neuronal death. The bulk motion comes from cardiac muscle fibers. Consider that the resting heart rate of the mouse is around 500 bpm to 700 bpm, and the slowest speed is 100 ms on the order of milliseconds [52]. For tissue dynamics imaging, 1600 sequential *en face* frames are captured in 10.6 s at the exact location in the sample. This can be sufficient for heart tissue dynamics by the FF-OCT system.

Comparing the conventional FF-OCT images in Fig. 9(a) and dynamic FF-OCT images in Fig. 9(b) in the marked location. The dynamic contrast presents low-frequency chamber and high-frequency cardiac muscle fibers. In addition, metabolism activities that come from mitochondria and myoglobin in cardiac muscle suggest dFFOCT offers more information than the morphological structures obtained by the FF-OCT image of heart tissue.

5. Discussion

A fractal-based computational compensation approach was proposed for correcting of depth-resolved aberrations with volumetric FF-OCT. Several comparisons and current limitations about the extension of aberration correction method, 3D inhomogeneous model in fractal analysis performance and determination of tissue dynamics with potential functions will be iscussed as following.

In parallel *enface* FF-OCT imaging, the defocus effect on contrast changes in the microscopic structures of the sample and the FF-OCT images need to be compensated by considering the change of local relative index of the sample itself, and sample-induced optical aberrations. For example, the focus shift can be removed on geometrical approximation with Eq. (5) in the case of monochromatic illumination and high NA. In this case, the radial spatially fractal dimension of *en face* FF-OCT images can be used for compensation computationally [53]. More than that, defocus-induced lateral resolution loss in Fourier-domain scanning OCT has also been compensated in several ways. One designed a depth-dependent lateral point spread function in a deconvolution filter to recover inverse phase terms in the frequency domain. The refocused lateral resolution enhancement can be seen in intensity image and birefringence and degree-of-polarization-uniformity(DOPU) images in polarization-sensitive sample [16,54]. The proposed fractal dimension filter can also be used for this defocus compensation because the inhomogeneous model hypothesis. The hypothesis holds the view that we consider sample contains refractive index inhomogeneities or the variations with sizes on a continuum range. It holds true because it has been shown that at the microscopic scale, tissue can be modeled as random continuous medium, and the properties of light scattered from random bulk media such as tissue are related to the spatial correlation of the fluctuations of the refractive index between any two points within tissue [14,55–59]. It can not only be appropriate for FF-OCT imaging modality since its subcellular three-dimensional high-resolution capability, but also can build model for tissue-induced high-order aberration or interact aberration. More simulation and experiments are ongoing, so far, it is the most proper model for real sample imaging for FF-OCT modality

A summary of experimentally measured fractal tissue parameters indicated a general trend of convergence range in human organs from 2.50 to 4.50 [51]. Although the fractal dimension and its related findings are measured and analyzed from a mouse, the biological scattering model is from the statistical properties of the refractive-index variations inhomogeneities medium. Therefore, the result can be extended to real human tissue. In addition, we are still working on building a human sample fractal dimension library but taking more time due to the need for more human samples.

The fractal refractive index for describing the turbulent fluctuations in tissue can be expressed by an autocorrelation function and its power spectral density. There are a few points of achieving fractal convergence range by controlling variables in multiple samples. First, J.M. Schmitt et al. proved that the observed spectral of refractive index variations from biological tissue over a range of scales fit the classic Kolmogorov model [14]. In this model, fractal dimension and length scale are the main variations to describe spectra shape. In our case, the resolution of FF-OCT imaging modality determines the length scale while the refraction index variations are the properties from the real sample [15,51]. As a result, the fractal convergence range can indicate similar quantitative properties of the same organs. Second, for better fractal analysis precision, images' increasingly spatial resolution takes computation time due to radial Fourier transform. The pre-trained fractal model takes one or two seconds. Once the fractal model was built, the computing time for one sample consisting of 1024 × 1024 × 400 data is about 20s using the tic-toc function with Matlab (16 GB memory, four performance, and four efficiency Cores, Apple M1, Mac Mini, Apple). Also, the fractal dimension slightly changed with resizing of *en face* images. We computed the three-dimension of 512 $pixel^3$ with a spatial resolution of 0.1 mm^{-1}. Third, one of the current limitations of depth-resolved fractal analysis in hardware comes from a depth of field limited by objective and penetration depth limited by the center wavelength. Our system allows 200 µm imaging depth for a sensitivity of about 70 dB. Higher NA (numerical aperture) of the objective and near-infrared band might be one selection for deep imaging.

After the proposed aberration compensation method, the temporal contrast imaging visualized the active region of both bulk and local motion. Several groups have achieved label-free, noninvasive depth-resolved intracellular motility by OCT signal. It was initially performed using time-domain full-field OCT by time-lapse sequence signal frequency analysis of OCT signal [3,46]. It was recently demonstrated using Fourier-domain OCT by analyzing the correlation decay speed of the OCT signal [39,60]. Fourier-domain full-field swept-source OCT also provides a prospect of characterizing the spatially-resolved temporal-frequency response of the nanometric photoreceptor optical path length change with stimulus light adapted [4]. The fractal analysis of FF-OCT signals regards the sample as an inhomogeneous refraction index containing spatial correlation scatterers within the system resolution range. In addition, the functional information contained in the decorrelation time, fractal dimension, or frequency-dependent parameters characterizing the dynamic signal between cells needs to be explored, which highlight the possibility of classifying the cell motility from different size of cell organelle by fractal-based dFFOCT signal in the future.

The selection of FF-OCT system parameters determines the performance of the dynamic signal. Flying bugs in onion and heart beating movement were recorded for the trade-off between camera framerate and exposure time required to use the camera's full dynamic range. The maximum attainable frame rate in fps (frames per second) cannot surpass one divided by the exposure time in seconds. On the one hand, more framerate means less total acquisition time, leading to more complexity in capturing the slow relative motions in the sample and fewer motion artifacts. On the other hand, more exposure time for one frame will increase system sensitivity and signal-to-noise ratio.

In tissue dynamics, the strong static scatters caused bulk motion, and metabolic scatters caused the relative motion. In the case of flying bugs in onion in mitosis, the bulk motion is the cell wall of the onion root tip during mitotic growth, while the relative motion comes from the observed flying micro bugs and onion cells. The flying micro bugs are randomly flying, and the averaged resolvable changes can be seen within one frame of 6.67 ms. It is a speed on the order of milliseconds. The measured average diameter of moving bugs is around 10-20 μm. Straight et al. used green fluorescent protein (GFP) to follow chromosome and spindle movements in living yeast cells by fluorescence microscopy. They observed that the separation of the centromeres showed a jump of 1.8 μm (average) in less than 26 s [61]. Nina Stromgren Allen et al. used computer-assisted video (AVEC-DIC, AVEC-POL, and fluorescence) microscopy to summarize the average velocity measurements for organelles and particles in the cytoplasm of onion epidermal cells [62]. Most of them are in µm per second, such as the mitochondrion of onion epidermal cells is about 3 μm/second. In this case, we may imply that organelles and particles in the cytoplasm of onion cells can theoretically move in three dimensional within a few seconds. We observed and visualized the dynamic signals by temporal-contrast-based FF-OCT images in 10.6 seconds. Please note that it is deduced that the dynamic contrast comes from the onion sample. In addition, we will try higher framerate sequential acquisition of FF-OCT frames at the same location and more subsequent statistical signal analysis methods that quantify the signal fluctuations to evaluate the intracellular activities within a few seconds [60]. In the case of heart-beating movement, the bulk motion is cardiac muscle fibers. In contrast, the relative motion comes from the ventricular chamber and cardiac muscle fibers in disappearing heart beating. Consider the resting heart rate of a mouse is around 500 bpm (beats per minute) to 700 bpm, and the slowest speed is 100 ms on the order of milliseconds [52]. As a result, we choose at most a 150 fps framerate camera. For tissue dynamics imaging, 1600 sequential *en face* frames are captured in 10.6 s at the exact location in the sample with a minimum exposure time of $10\mu s$.

6. Conclusion

In conclusion, fitting depth-resolved changes in fractal parameters is a quantitative method in defocus compensation and contrast augmentation using FF-OCT. First, the refocused distance observed from the in-depth fractal dimension model of the mouse organ indicated the defocused amount. The most optimal fractal model for each mouse organ was selected by fitting linear curves and in-focus data in strategy. Seven mouse organs' intensity images demonstrate that refocusing can be optimized with a deconvolution phase compensation filter. By separating the tissue-induced optical aberrations, the fractal-based refocusing compensation shows enhanced contrast in *ex vivo* mouse organ imaging. Another finding is that the temporal contrast was fused with FF-OCT images and can be used to monitor dynamic scatterers in mouse organs. The proposed fractal-based contrast augmented images show subcellular resolution recording of dynamic scatters of the growing-up onion cell wall and some micro activities. In addition, low-frequency chamber and high-frequency cardiac muscle fibers from *ex vivo* mouse heart tissue. The metabolism activities from mitochondria and myoglobin in cardiac muscle suggest dFFOCT offers cell motility contrast over the morphological structures obtained by conventional FF-OCT images. However, temperature variations and environmental vibrations affect the cell motility contrast that cannot quantify the different degrees of cell viability. Also, the liquid draft generated motion artifacts when moving the translation stage. We will keep measuring the metabolism activities in the human sample's cardiac muscle fiber and vascular chamber to obtain the real-time non-invasive heart frequency and respiratory rate with the FF-OCT system.

Funding. National Natural Science Foundation of China (62005123, 60978069, 61275198); China Scholarship Council (202106845011); Natural Science Foundation of Jiangsu Province (BK20190455); Nanjing University of Science and Technology (30919011226); Fundamental Research Funds for the Central Universities (30920010003).

Acknowledgments. The study was approved by the Ethics Committee of Wuxi No. 3 People's Hospital. I would like to thank Prof. Wanrong Gao for his long-term mentorship. I would like to thank Chen Jianjian (Center of Interventional Radiology and Vascular Surgery, Department of Radiology, Zhongda Hospital, Medical School, Southeast University, Nanjing, China) for his kind help in sample preparations. I would also like to thank my life partner Yingying for the company in the dark period of my career.

Disclosures. The authors declare no conflicts of interest.

Data availability. Data underlying the results presented in this paper are not publicly available at this time but may be obtained from the authors upon reasonable request.

References

1. E. Beaurepaire, A. C. Boccara, M. Lebec, L. Blanchot, and H. Saint-Jalmes, "Full-field optical coherence microscopy," Opt. Lett. **23**(4), 244–246 (1998).
2. A. Dubois, L. Vabre, A.-C. Boccara, and E. Beaurepaire, "High-resolution full-field optical coherence tomography with a linnik microscope," Appl. Opt. **41**(4), 805–812 (2002).
3. J. Scholler, K. Groux, O. Goureau, J.-A. Sahel, M. Fink, S. Reichman, C. Boccara, and K. Grieve, "Dynamic full-field optical coherence tomography: 3d live-imaging of retinal organoids," Light: Sci. Appl. **9**(1), 140 (2020).
4. S. Tomczewski, P. Wegrzyn, D. Borycki, E. Auksorius, M. Wojtkowski, and A. Curatolo, "Light-adapted flicker optoretinograms captured with a spatio-temporal optical coherence-tomography (stoc-t) system," Biomed. Opt. Express **13**(4), 2186–2201 (2022).
5. E. Auksorius, D. Borycki, P. Wegrzyn, B. L. Sikorski, K. Lizewski, I. Zickiene, M. Rapolu, K. Adomavicius, S. Tomczewski, and M. Wojtkowski, "Spatio-temporal optical coherence tomography provides full thickness imaging of the chorioretinal complex," iScience **25**(12), 105513 (2022).
6. D. Valente, K. V. Vienola, R. J. Zawadzki, and R. S. Jonnal, "Kilohertz retinal ff-ss-oct and flood imaging with hardware-based adaptive optics," Biomed. Opt. Express **11**(10), 5995–6011 (2020).

7. H. Spahr, D. Hillmann, C. Hain, C. Pfäffle, H. Sudkamp, G. Franke, and G. Hüttmann, "Imaging pulse wave propagation in human retinal vessels using full-field swept-source optical coherence tomography," Opt. Lett. **40**(20), 4771–4774 (2015).
8. M. Davidson, K. Kaufman, I. Mazor, and F. Cohen, "An application of interference microscopy to integrated circuit inspection and metrology," in *Integrated Circuit Metrology, Inspection, and Process Control*, vol. 775 (SPIE, 1987), pp. 233–249.
9. G. S. Kino and S. S. Chim, "Mirau correlation microscope," Appl. Opt. **29**(26), 3775–3783 (1990).
10. P. de Groot and X. C. de Lega, "Signal modeling for low-coherence height-scanning interference microscopy," Appl. Opt. **43**(25), 4821–4830 (2004).
11. A. Safrani and I. Abdulhalim, "Spatial coherence effect on layer thickness determination in narrowband full-field optical coherence tomography," Appl. Opt. **50**(18), 3021–3027 (2011).
12. A. Safrani and I. Abdulhalim, "Ultrahigh-resolution full-field optical coherence tomography using spatial coherence gating and quasi-monochromatic illumination," Opt. Lett. **37**(4), 458–460 (2012).
13. W. Gao, "Effects of temporal and spatial coherence on resolution in full-field optical coherence tomography," J. Mod. Opt. **62**(21), 1764–1774 (2015).
14. J. Schmitt and G. Kumar, "Turbulent nature of refractive-index variations in biological tissue," Opt. Lett. **21**(16), 1310–1312 (1996).
15. W. Gao and Y. Zhu, "Fractal analysis of en face tomographic images obtained with full field optical coherence tomography," Ann. Phys. **529**(3), 1600216 (2017).
16. Y. Yasuno, J.-i. Sugisaka, Y. Sando, Y. Nakamura, S. Makita, M. Itoh, and T. Yatagai, "Non-iterative numerical method for laterally superresolving fourier domain optical coherence tomography," Opt. Express **14**(3), 1006–1020 (2006).
17. D. Hillmann, H. Spahr, C. Hain, H. Sudkamp, G. Franke, C. Pfäffle, C. Winter, and G. Hüttmann, "Aberration-free volumetric high-speed imaging of in vivo retina," Sci. Rep. **6**(1), 35209 (2016).
18. H. Schulz-Hildebrandt, M. Münter, M. Ahrens, H. Spahr, D. Hillmann, P. König, and G. Hüttmann, "Coherence and diffraction limited resolution in microscopic oct by a unified approach for the correction of dispersion and aberrations," in *2nd Canterbury Conference on OCT with Emphasis on Broadband Optical Sources*, vol. 10591 (SPIE, 2018), pp. 145–151.
19. W. Gao, "Image contrast reduction mechanism in full-field optical coherence tomography," J. Microsc. **261**(3), 199–216 (2016).
20. A. Dubois, "Focus defect and dispersion mismatch in full-field optical coherence microscopy," Appl. Opt. **56**(9), D142–D150 (2017).
21. V. Mazlin, P. Xiao, E. Dalimier, K. Grieve, K. Irsch, J.-A. Sahel, M. Fink, and A. C. Boccara, "In vivo high resolution human corneal imaging using full-field optical coherence tomography," Biomed. Opt. Express **9**(2), 557–568 (2018).
22. V. Barolle, J. Scholler, P. Mecê, J.-M. Chassot, K. Groux, M. Fink, A. Claude Boccara, and A. Aubry, "Manifestation of aberrations in full-field optical coherence tomography," Opt. Express **29**(14), 22044–22065 (2021).
23. S. Labiau, G. David, S. Gigan, and A. C. Boccara, "Defocus test and defocus correction in full-field optical coherence tomography," Opt. Lett. **34**(10), 1576–1578 (2009).
24. G. Min, J. W. Kim, W. J. Choi, and B. H. Lee, "Correction of defocused images in full-field optical coherence tomography using digital holography," in *Three-Dimensional and Multidimensional Microscopy: Image Acquisition and Processing XVIII*, vol. 7904 (SPIE, 2011), pp. 280–286.
25. M. Blavier, M. Glanc, and G. Rousset, "Analysis of the impact of optical aberrations in en-face full-field oct microscopy," Opt. Express **29**(2), 2204–2226 (2021).
26. A. Kumar, W. Drexler, and R. A. Leitgeb, "Subaperture correlation based digital adaptive optics for full field optical coherence tomography," Opt. Express **21**(9), 10850–10866 (2013).
27. A. Kumar, W. Drexler, and R. A. Leitgeb, "Numerical focusing methods for full field oct: a comparison based on a common signal model," Opt. Express **22**(13), 16061–16078 (2014).
28. P. Pande, Y.-Z. Liu, F. A. South, and S. A. Boppart, "Automated computational aberration correction method for broadband interferometric imaging techniques," Opt. Lett. **41**(14), 3324–3327 (2016).
29. D. Borycki, E. Auksorius, P. Wegrzyn, and M. Wojtkowski, "Computational aberration correction in spatiotemporal optical coherence (stoc) imaging," Opt. Lett. **45**(6), 1293–1296 (2020).
30. A. Dunn and R. Richards-Kortum, "Three-dimensional computation of light scattering from cells," IEEE J. Sel. Top. Quantum Electron. **2**(4), 898–905 (1996).
31. A. K. Dunn, C. Smithpeter, A. J. Welch, and R. Richards-Kortum, "Sources of contrast in confocal reflectance imaging," Appl. Opt. **35**(19), 3441–3446 (1996).
32. Y. Pan, R. Birngruber, J. Rosperich, and R. Engelhardt, "Low-coherence optical tomography in turbid tissue: theoretical analysis," Appl. Opt. **34**(28), 6564–6574 (1995).
33. Y. Nakamura, J.-i. Sugisaka, Y. Sando, T. Endo, M. Itoh, T. Yatagai, and Y. Yasuno, "Complex numerical processing for in-focus line-field spectral-domain optical coherence tomography," Jpn. J. Appl. Phys. **46**(4A), 1774–1778 (2007).
34. Y. Zhu, W. Gao, Z. Guo, Y. Zhou, and Y. Zhou, "Liver tissue classification of en face images by fractal dimension-based support vector machine," J. Biophotonics **13**(4), e201960154 (2020).
35. J. W. Baish and R. K. Jain, "Fractals and cancer," Cancer Res. **60**(14), 3683–3688 (2000).

36. Y. Zhu and W. Gao, "Single-shot wavelength-independent phase-shifting method for full-field optical coherence tomography," Appl. Opt. **58**(4), 806–813 (2019).
37. W. George, *Wave Propagation: Wave Propagation in a Turbulent Medium* vol. 285 (McGraw-Hill, 1961).
38. U. Tricoli and R. Carminati, "A model for full-field optical coherence tomography in scattering media," in *Biomedical Spectroscopy, Microscopy, and Imaging*, vol. 11359 (International Society for Optics and Photonics, 2020), p. 113590M.
39. W. Gao, "Fourier spectrum analysis of full-field optical coherence tomography for tissue imaging," Proc. R. Soc. London, Ser. A **471**(2179), 20150099 (2015).
40. C. J. R. Sheppard, "Scattering by fractal surfaces with an outer scale," Opt. Commun. **122**(4-6), 178–188 (1996).
41. J. D. Rogers, A. J. Radosevich, J. Yi, and V. Backman, "Modeling light scattering in tissue as continuous random media using a versatile refractive index correlation function," IEEE J. Sel. Top. Quantum Electron. **20**(2), 173–186 (2014).
42. P. Giannios, K. G. Toutouzas, M. Matiatou, K. Stasinos, M. M. Konstadoulakis, G. C. Zografos, and K. Moutzouris, "Visible to near-infrared refractive properties of freshly-excised human-liver tissues: marking hepatic malignancies," Sci. Rep. **6**(1), 27910 (2016).
43. Y. Zhu, W. Gao, and Y. Guo, "A method of improving imaging quality of full-field optical coherence tomography," Acta Opt. Sin. **35**(5), 0517001 (2015).
44. X. Wu and W. Gao, "Dispersion analysis in micron resolution spectral domain optical coherence tomography," J. Opt. Soc. Am. B **34**(1), 169–177 (2017).
45. G. T. McNeil, "Metrical fundamentals of underwater lens system," Opt. Eng. **16**(2), 162128 (1977).
46. C. Apelian, F. Harms, O. Thouvenin, and A. C. Boccara, "Dynamic full field optical coherence tomography: subcellular metabolic contrast revealed in tissues by interferometric signals temporal analysis," Biomed. Opt. Express **7**(4), 1511–1524 (2016).
47. J. Scholler, "Motion artifact removal and signal enhancement to achieve in vivo dynamic full field oct," Opt. Express **27**(14), 19562–19572 (2019).
48. H. Tian, F. Tang, W. Gao, and Y. Zhu, "Review on dynamic scattered light measurement in full-field optical coherence tomography," Chin. J. Laser **49**, 0507202 (2022).
49. M. Endres, S. Namura, M. Shimizu-Sasamata, C. Waeber, L. Zhang, T. Gomez-Isla, B. T. Hyman, and M. A. Moskowitz, "Attenuation of delayed neuronal death after mild focal ischemia in mice by inhibition of the caspase family," J. Cereb. Blood Flow Metab. **18**(3), 238–247 (1998).
50. M. Jain, N. Shukla, M. Manzoor, S. Nadolny, and S. Mukherjee, "Modified full-field optical coherence tomography: A novel tool for rapid histology of tissues," J. Pathol. Inform. **2**(1), 28 (2011).
51. A. K. Glaser, Y. Chen, and J. T. Liu, "Fractal propagation method enables realistic optical microscopy simulations in biological tissues," Optica **3**(8), 861–869 (2016).
52. D. A. Kass, J. M. Hare, and D. Georgakopoulos, "Murine cardiac function," Circ. Res. **82**(4), 519–522 (1998).
53. Y.-Z. Liu, F. A. South, Y. Xu, P. S. Carney, and S. A. Boppart, "Computational optical coherence tomography [invited]," Biomed. Opt. Express **8**(3), 1549–1574 (2017).
54. L. Zhu, S. Makita, D. Oida, A. Miyazawa, K. Oikawa, P. Mukerjee, A. Lichtenegger, M. Distel, and Y. Yasuno, "Computational refocusing of jones matrix polarization-sensitive optical coherence tomography and investigation of defocus-induced polarization artifacts," Biomed. Opt. Express **13**(5), 2975–2994 (2022).
55. M. Xu and R. R. Alfano, "Fractal mechanisms of light scattering in biological tissue and cells," Opt. Lett. **30**(22), 3051–3053 (2005).
56. M. Hunter, V. Backman, G. Popescu, M. Kalashnikov, C. W. Boone, A. Wax, V. Gopal, K. Badizadegan, G. D. Stoner, and M. S. Feld, "Tissue self-affinity and polarized light scattering in the born approximation: a new model for precancer detection," Phys. Rev. Lett. **97**(13), 138102 (2006).
57. C. J. Sheppard, "Fractal model of light scattering in biological tissue and cells," Opt. Lett. **32**(2), 142–144 (2007).
58. J. D. Rogers and V. Backman, "Nonscalar elastic light scattering from continuous random media in the born approximation," Opt. Lett. **34**(12), 1891–1893 (2009).
59. W. Gao, "Spectral changes of the light produced by scattering from tissue," Opt. Lett. **35**(6), 862–864 (2010).
60. I. Abd El-Sadek, A. Miyazawa, L. Tzu-Wei Shen, S. Makita, S. Fukuda, T. Yamashita, Y. Oka, P. Mukherjee, S. Matsusaka, T. Oshika, H. Kano, and Y. Yasuno, "Optical coherence tomography-based tissue dynamics imaging for longitudinal and drug response evaluation of tumor spheroids," Biomed. Opt. Express **11**(11), 6231–6248 (2020).
61. A. F. Straight, W. F. Marshall, J. W. Sedat, and A. W. Murray, "Mitosis in living budding yeast: anaphase a but no metaphase plate," Science **277**(5325), 574–578 (1997).
62. N. S. Allen and D. T. Brown, "Dynamics of the endoplasmic reticulum in living onion epidermal cells in relation to microtubules, microfilaments, and intracellular particle movement," Cell Motil. **10**(1-2), 153–163 (1988).